ADVANCED MATERIALS TECHNOLOGIES
www.advmattechnol.de

Double-Sided Graphene-Enhanced Raman Scattering and Fluorescence Quenching in Hybrid Biological Structures

George Sarau, Christoph Daniel, Martin Heilmann, Gerd Leuchs, Kerstin Amann, and Silke H. Christiansen*

Due to their large contact and loading surfaces as well as high sensitivities to chemical changes, graphene-based materials (GBMs) are increasingly being employed into novel nanomedicine technologies. Here biomolecule—monolayer graphene—kidney tissue hybrid structures are studied using mapping micro-Raman and fluorescence spectroscopies. Because in this configuration graphene interacts with molecules on both sides, a double-sided graphene-enhanced Raman scattering (GERS) effect up to ≈10.1 is found for biomolecules adsorbed on graphene and amino acids in the kidney tissue below graphene. Moreover, graphene causes an efficient autofluorescence quenching (FLQ) up to ≈20% emitted by the kidney tissue. Despite the complexity of such layered materials, the intriguing simultaneous occurrence of double-sided GERS (a new development of GERS) and FLQ phenomena can be well explained by suitable molecular structure and energy level alignment between molecules and graphene. These result in effective charge transfer mediated by non-covalent interactions as indicated by correlative strain, doping, and defect analyses in graphene based on the Raman data and energy level calculations. Last, the advantages of using graphene over standard photobleaching are demonstrated. This work can be extended to other macromolecular entities toward integrating GBMs in versatile drug delivery, imaging, and sensing devices.

1. Introduction

Biomedical applications of graphene-based materials (GBMs) including antibacterial and photothermal anticancer therapy, tissue engineering, targeted gene and drug delivery, bioimaging, biosensing, and so on are currently attracting great interest in the emerging area of nanomedicine technologies.[1–3] These exciting functionalities exploit unique properties of GBMs such as large photoresponse and loading surface, excellent biocompatibility, and effective non-covalent interaction with various types of biomolecules present in drugs, cells, and tissues.[4–8] Raman spectroscopy has emerged as a powerful analytical method particularly when GBMs act as carrier, bioimaging, and biosensing platforms being label-free, non-destructive, and highly informative.[8–11] Plasmonic metal nanoparticles attached to GBMs are commonly used to increase the intrinsic Raman signals of both GBMs and biomolecules in close contact with the graphene sheets based on the surface enhanced Raman scattering (SERS) effect.[12–15] Nevertheless, the SERS technique can lack quantitative, repeatable, and stable enhanced Raman signal mostly because of a non-uniform distribution of the "hot spots" and chemical changes of the metal nanoparticles and molecules during laser irradiation due to increased photo-induced damage.[16–18]

Graphene enhanced Raman scattering (GERS) represents a robust alternative to SERS, in which graphene itself serves as a uniform Raman enhancement surface for the adsorbed molecules that exhibit clean and reproducible Raman spectra. The GERS effect shows a peculiar molecular selectivity implying appropriate alignment of the highest occupied and lowest uncopied molecular orbitals (HOMO and LUMO) as well as suitable molecular symmetry relative to the Fermi level (E_F) of graphene and its planar structure, respectively.[17–20] Other studies show that graphene can also be used as a fluorescence quenching (FLQ) surface for fluorescent molecules placed on top of it.[21–24] The GERS and FLQ effects

G. Sarau, S. H. Christiansen
Fraunhofer Institute for Ceramic Technologies and Systems IKTS
Äußere Nürnberger Str. 62, 91301 Forchheim, Germany
E-mail: george.sarau@ikts.fraunhofer.de

The ORCID identification number(s) for the author(s) of this article can be found under https://doi.org/10.1002/admt.202100385.

[+]Present address: IMEC Kapeldreef 75, 3001 Leuven, Belgium

DOI: 10.1002/admt.202100385

G. Sarau, M. Heilmann,[+] G. Leuchs, S. H. Christiansen
Leuchs Emeritus Group
Max Planck Institute for the Science of Light
Staudtstr. 2, 91058 Erlangen, Germany

G. Sarau, S. H. Christiansen
Institute for Nanotechnology and Correlative Microscopy eV INAM
Äußere Nürnberger Str. 62, 91301 Forchheim, Germany

C. Daniel, K. Amann
Department of Nephropathology
Friedrich-Alexander-Universität Erlangen-Nürnberg (FAU)
Krankenhausstr. 8–10, 91054 Erlangen, Germany

S. H. Christiansen
Physics Department
Freie Universität Berlin
Arnimallee 14, 14195 Berlin, Germany

were separately reported for individual molecules mainly on single-layer graphene supported by flat SiO_2/Si substrates. However, the target cells and tissues contain different sorts of biomolecules arranged in complex molecular structures and have uneven contact surfaces with biomolecule loaded GBMs as usually employed in nanomedicine.[4–8] Such intricate combinations of materials are expected to result in distinct, multiple biomolecule—graphene interactions that have not been really addressed so far.

Here we use Raman and fluorescence (FL) spectroscopies complemented by energy level calculations to investigate hybrid structures consisting of biomolecule—monolayer graphene—kidney tissue layers. Both biocompatible nitrocellulose molecules and kidney tissue show characteristic Raman peaks with mean enhancement factors (EFs) as high as 10 indicating double-sided GERS. Moreover, graphene itself displays increased G and 2D Raman peaks with mean EFs of up to 6.8 and contributes to ≈20% quenching of the kidney tissue autofluorescence. In contrast to graphene-induced FLQ, standard photobleaching causes ≈twofold decrease in the intensity of kidney Raman peaks. The double-sided GERS, graphene Raman enhancement, and FLQ effects in this particular or similar materials configurations were not reported up to now based on our literature research. This study provides fundamental insights into the properties of graphene materials when located between biomolecules that can be used to further advance its functionalities in biomedical applications mentioned earlier.

2. Results and Discussion

2.1. Biomolecule—Monolayer Graphene—Kidney Tissue Hybrid Structures

In order to correlate the changes in the graphene properties caused by interactions with molecules on both sides of graphene, we investigated successive materials configurations corresponding to important stages in the preparation of samples. **Figure 1**a displays a schematic representation of the constituting layers, laser excitation at normal incidence, and backscattering collection of the resulting FL and Raman signals. First, the supporting Si wafer was covered by a 100 nm thick Ni film, which suppresses the Si Raman background, exhibits a flat spectrum, and acts as a metallic mirror coating increasing the Raman intensity of the kidney tissue, graphene, and molecules both in excitation and detection (Figures S1 and S2, Supporting Information).[25,26] Second, ≈5 µm thick sections of cryo-fixed human, healthy kidney tissue were placed on the Ni film, denoted Ki/Ni, without any staining to avoid spectral artifacts. Third, large-area, high quality predominantly single-layer graphene films overlaid with biocompatible nitrocellulose molecules were transferred onto the Ni film and kidney tissue, denoted Mo/Gr/Ni and Mo/Gr/Ki/Ni, respectively. The biocompatibility of nitrocellulose is demonstrated by its extensive use in biomedicine as membrane for protein blotting.[27,28]

These probe biomolecules are the remains from a newly developed collodion-mediated transfer method that works at room temperature, in contrast to the well-established, temperature-intensive PMMA-assisted transfer process, so that heat-induced changes of the kidney tissue, graphene, and molecules can be excluded in our case (Experimental Section).[29] Thus, our hybrid structures can be regarded as a model system for drug delivery, imaging, and sensing applications down to organs (here kidney). The optical microscope image in Figure 1b indicates that monolayer graphene conforms along the uneven kidney tissue surface providing an interfacing area.[30] For a direct comparison, we employed the same procedure to transfer graphene onto standard 300 nm thick SiO_2/Si substrates, denoted Mo/Gr/SiO_2. Interestingly, the Raman enhancement produced by the well-known SiO_2 interference effect can be compensated to a large extent up to 92% by the Ni mirror effect (Figure S3, Supporting Information).[31]

2.2. FL and Raman Spectroscopies

Figure 2 shows that single-layer graphene can simultaneously induce autofluorescence quenching and Raman enhancement

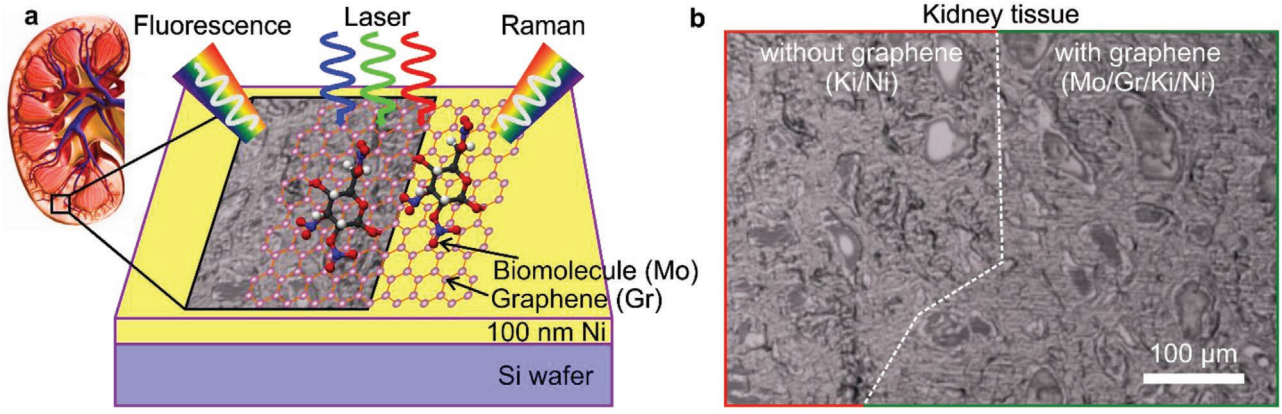

Figure 1. a) Sketch of the biomolecule (Mo)—monolayer graphene (Gr)—kidney tissue (Ki) hybrid structures on a Ni mirror film illustrating different materials configurations involving Ni, Ki/Ni, Mo/Gr/Ni, and Mo/Gr/Ki/Ni, probed by fluorescence and micro-Raman spectroscopies. Mo stands for biocompatible nitrocellulose molecules from the graphene transfer. b) Optical microscopy image of the kidney tissue without (left side) and with graphene atop (right side). The single-layer graphene is visible through its slightly light absorption. Due to its planar structure and mechanical flexibility, graphene can follow the irregular kidney tissue surface.

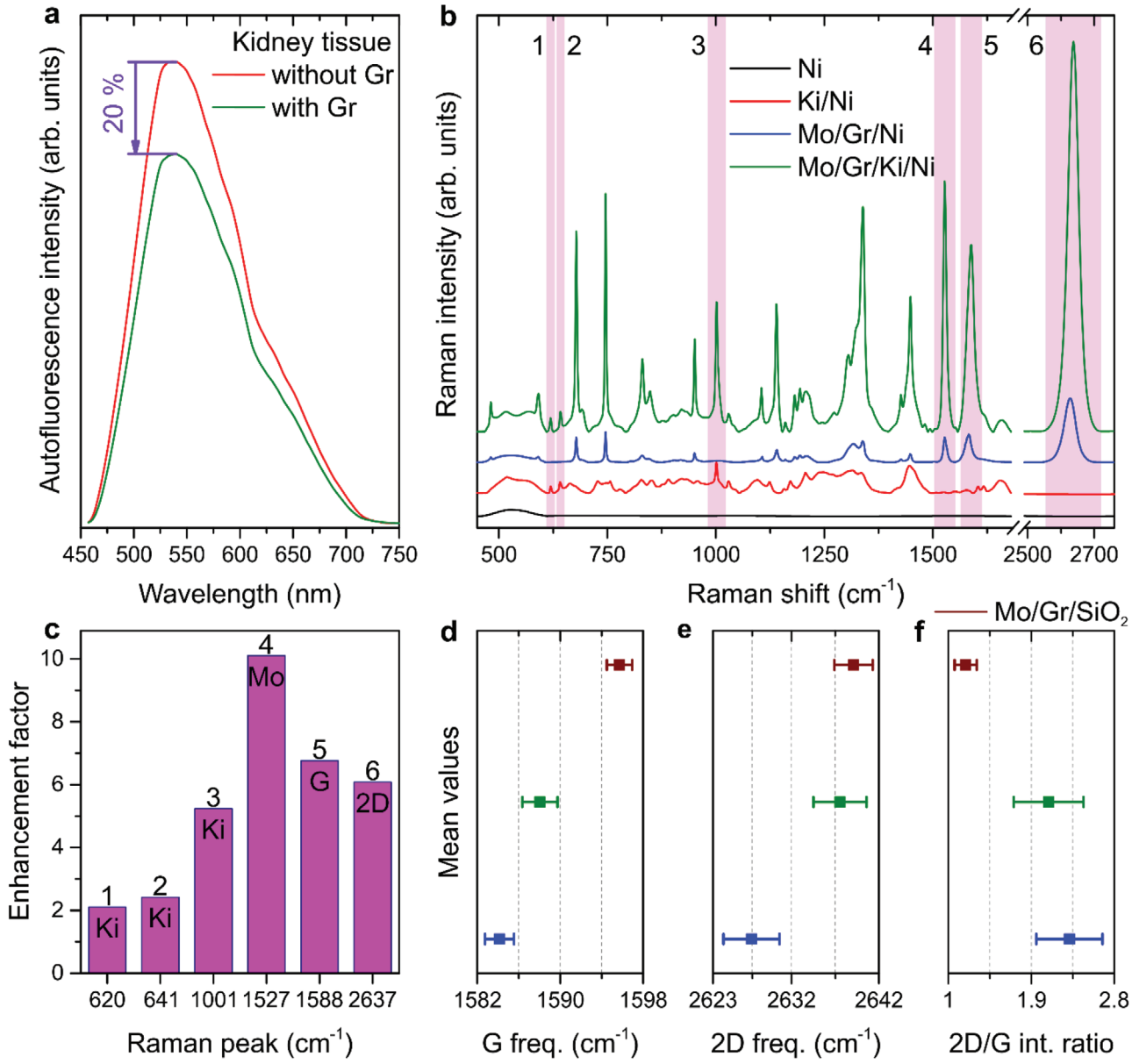

Figure 2. a) Graphene-induced quenching of kidney tissue autofluorescence excited with a 457 nm laser. b) Mean Raman spectra of layered materials after removing the autofluorescence background obtained with a 660 nm laser. The spectra were vertically shifted for clarity. c) Mean Raman enhancement factors for two amino acids (tyrosine and phenylalanine) in the kidney tissue below graphene (Ki), biocompatible nitrocellulose molecules above graphene (Mo), and graphene itself (G, 2D) attributed to the double-sided GERS effect. The six non-overlapping Raman peaks are highlighted in (b). d–f) Mean values of some relevant Raman parameters for single-layer graphene on used substrates: Ni, Ki, and SiO_2 as reference. These and other Raman peak features are listed in Table S1, Supporting Information.

even in complex macromolecular systems like tissues, both effects (FLQ and GERS) being explained by charge transfer between molecules and graphene.[20,22,32] Broad autofluorescence emission occurs from naturally fluorescent tissue molecules and/or due to chemical changes of molecules during fixation and processing steps. There are mainly two approaches to minimize autofluorescence, employing chemicals and photobleaching; however, these treatments can modify tissue integrity irreversibly.[33,34] Remarkably, we observed an efficient reduction up to 20% of the autofluorescence signal emitted by the kidney tissue resulting from the contact with monolayer graphene as shown by the mean FL spectra in Figure 2a. This finding points toward a novel strategy to achieve FLQ in tissues using graphene that will be later compared to standard photobleaching.

Figure 2b reveals the evolution of the mean Raman spectra when stacking various materials after subtracting the FL background (Figure S2, Supporting Information). Given the multitude of Raman bands in our spectra, we focused on six non-overlapping Raman peaks related to each material and evaluated their mean EFs displayed in Figure 2c. These peaks are attributed to amino acids in the kidney tissue (tyrosine at ≈620 and ≈641 cm^{-1}, phenylalanine at ≈1001 cm^{-1}), nitrocellulose

molecules at ≈1527 cm^{-1}, and graphene (G at ≈1588 cm^{-1} and 2D at ≈2637 cm^{-1}). Detailed assignments of the Raman peaks can be found in literature.[35–38] It should be noted, however, that the original Raman peaks of isolated amino acids can be affected to some extent when folded in large proteins as part of cells and tissues.[39] The EF values varying from ≈2.1 to ≈10.1 are in the range of GERS, which is based on the chemical enhancement mechanism implying molecule-graphene coupling through non-covalent interactions leading to mutual charge exchange. Van der Waals, π-π stacking, and hydrophobic interactions are primarily considered responsible for the biomolecular interplay with graphene and thus for the GERS and FLQ effects.[20,32,40–42]

The GERS EFs were obtained by dividing the mean Raman intensities, since the same graphene and tissue layers as well as identical transfer procedures were employed for different materials configurations ensuring similar mean molecule concentrations above and below graphene with expected uniform spatial deviations (Figure S4, Supporting Information).[20] Notably, not only the adsorbed molecules on top of graphene (peak 4) corresponding to the typical geometry in GERS experiments, but also the kidney molecules underneath graphene (peaks 1–3) exhibit EFs indicating a new development of GERS that we called double-sided graphene-enhanced Raman scattering. These results are in line with the work of Zhang et al. where a bifacial Raman enhancement was observed for copper phthalocyanine (CuPc) probe molecules at both interfaces of mechanically exfoliated single-layer graphene.[32] Moreover, the graphene itself is affected by the presence of top and bottom molecules resulting in Raman enhancements (peaks 5, 6) and spectral changes that will be next correlated to doping, defect, and strain levels in the graphene films.[29]

The mean values of relevant Raman fitting parameters, intensity ratios, and their standard deviations are summarized in Figure 2d–f and Table S1, Supporting Information. We measured upshifts of ≈4 and ≈10 cm^{-1} for the frequencies (positions) of G (ω_G) and 2D (ω_{2D}) peaks of graphene, respectively, in contact with the kidney tissue versus graphene on Ni (Figure 2d,e). These results indicate hole doping of graphene and confirm the charge transfer interactions between kidney molecules and graphene, which is consistent with similar trends documented in literature.[31,40,43–45] The p-type doping of graphene is further supported by the decrease in I_{2D}/I_G from ≈2.5 to ≈2.1 (Figure 2f) at comparable low defect densities as revealed by nearly identical I_D/I_G of ≈0.15 and ≈0.16 without and with kidney tissue, respectively.[29] For the sake of comparison, we also studied the Raman response of graphene transferred under the same experimental conditions on standard SiO_2/Si substrates. Upshifts of ≈11 and ≈12 cm^{-1} for ω_G and ω_{2D}, respectively, as compared to graphene on Ni and a decrease in I_{2D}/I_G to ≈1.2 attributed to hole doping accompanied by virtually unchanged defect density as pointed out by I_D/I_G of ≈0.17 were observed.

2.3. Strain and Doping Correlations

Given the homogeneous defectiveness in our graphene layers, it is possible to separate and quantify doping and strain using the correlation plot ω_G versus ω_{2D} as demonstrated in **Figure 3**a. This approach is based on reported experimental dependences of ω_G and ω_{2D} at varying strain/doping and constant doping/strain (black/red solid lines, red dashed line is the linear fit to the red solid line).[29,46,47] By intersecting the magenta dashed lines with the black solid line and the red dashed line, mean biaxial, in-plane strain values, and doping concentrations are extracted for each type of sample (Table S1, Supporting Information). Negligible residual strains were found on all substrates, tensile on Ni ($\varepsilon \approx 0.036\%$) and SiO_2 ($\varepsilon \approx 0.006\%$) and compressive on kidney tissues ($\varepsilon \approx -0.025\%$), which is expected for as-transferred single-layer graphene without thermal treatments and covalent doping.[29] Interestingly, the strain differences between flat (Ni, SiO_2) and irregular (kidney tissue) substrates are minor indicating that large-area monolayer graphene can also follow uneven surfaces and thus form a continuous, closed contact down to orbital overlapping. This enables carrier-exchanged paths between graphene and surface atoms or molecules in the underlying substrates. Indeed, distinct hole doping levels were derived for graphene transferred on different substrates: $p \approx -3.8 \times 10^{12}$ cm^{-2} on Ni, $\approx -4.01 \times 10^{12}$ cm^{-2} on kidney tissue, and $\approx -10.28 \times 10^{12}$ cm^{-2} on SiO_2.

The strain-doping development in Figure 3a is further corroborated by additional correlation plots of other Raman parameters displayed in Figure 3b–e including (I_{2D}/I_G, ω_G), (Γ_G, ω_G), (I_{2D}/I_G, ω_{2D}), and (Γ_{2D}, ω_{2D}) with Γ_G and Γ_{2D} standing for the full-width at half-maximum (fwhm) of the G and 2D peaks. Their mean values along with the standard deviations are summed up in Table S1, Supporting Information. It has been shown that ω_G and ω_{2D} exhibit dissimilar responses to doping and strain variations, respectively.[29,46,48] In contrast, we noticed similar, mainly doping-induced dependences of ω_G and ω_{2D} since our graphene films are practically strain-free. The upshifts of the G and 2D peaks accompanied by reductions in I_{2D}/I_G (Figure 3b,d) as well as in Γ_G and Γ_{2D} (Figure 3c,e) are in excellent agreement with increasing p-type doping concentrations in the graphene layers as extracted from Figure 3a (Ni → kidney tissue → SiO_2). Furthermore, narrow Γ_G values (≈16.89 cm^{-1} on Ni, ≈15.32 cm^{-1} on kidney tissue, and ≈11.89 cm^{-1} on SiO_2) indicate low structural disorder in the graphene lattice, in line with minor defect densities (small I_D/I_G) and strain levels as revealed above.[29,46]

2.4. Energy-Level Alignment and Molecular Structure

There are two main molecular selection rules that determine separately and/or concurrently the efficacy of the GERS and FLQ phenomena. On the one hand, the HOMO and LUMO energy levels of the molecules should be located in the right energy range with respect to the Fermi level E_F of graphene to allow charge transfer. On the other hand, the structure of the molecules should follow the symmetry of graphene to minimize the space between them and thus to strengthen the molecule-graphene coupling.[20,40] Thus, the closer the alignment of energy levels and distance between graphene and molecules, the more effective the charge transfer at the interface between them, and the larger the FLQ and GERS effects. The charge transfer paths involve the wave function overlap as well as electron-photon and electron-phonon coupling between graphene and molecules, while the charge shift direction is difficult to assess because of the presence of different molecules on both

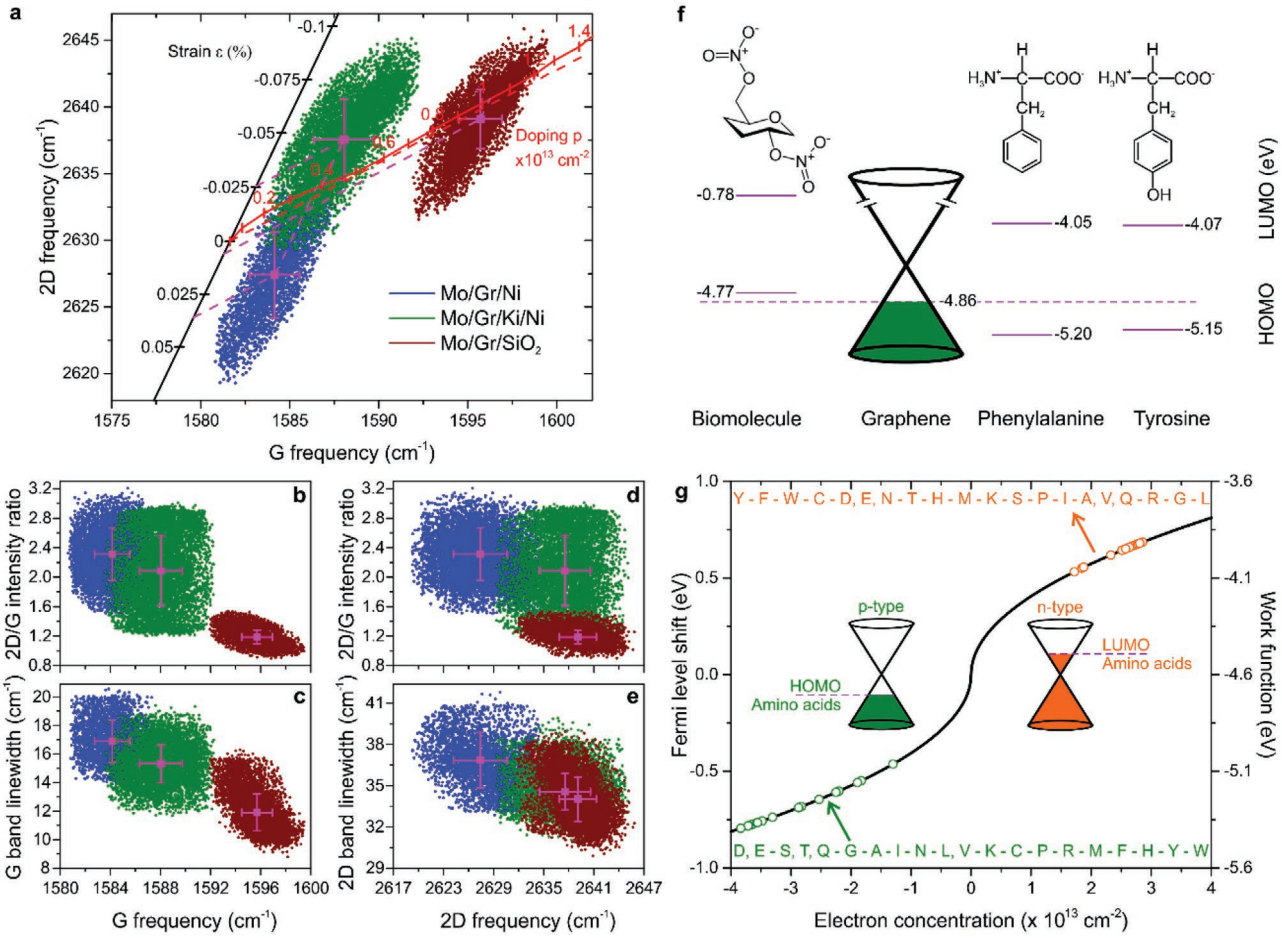

Figure 3. a) Correlation plot used to separately quantify strain and doping levels in graphene based on published dependences measured by modifying strain/doping at fixed doping/strain (black/red solid lines, red dashed line is the linear fit to the red solid line). b–e) Extra correlation plots that qualitatively support the strain—doping development in (a). The related data in (a–e) are summarized in Table S1, Supporting Information. f) Molecular structures (first row) and energy level alignment (second row) between the Fermi level of our p-doped graphene (dashed purple line) and the HOMO/LUMO energies (purple solid lines) of biocompatible nitrocellulose molecules and two amino acids in the kidney tissue. g) Calculated doping concentrations in monolayer graphene that are needed, in principle, to align its Fermi level and work function with the HOMO/LUMO energies of 20 amino acids usually present in biological molecules. The exact values and abbreviations can be found in Tables S2 and S3, Supporting Information.

sides of graphene.[19,32] The combination of these factors for our biomolecule—monolayer graphene—kidney tissue hybrid structures is illustrated in Figure 3f. Knowing the hole doping concentration p ≈ –4.01 × 10^{12} cm^{-2} in graphene on kidney tissues evaluated by Raman, we estimated an E_F down shift of ≈–0.26 eV using $E_F(n) = \hbar|v_F|\sqrt{\pi n}$, where n is the carrier concentration in cm^{-2}, ħ = 6.58 × 10^{-16} eVs is the reduced Planck's constant, and $|v_F| = 1.1 \times 10^6$ ms^{-1} is the Fermi velocity. Consequently, the work function of graphene with respect to the vacuum level changes from Φ_{Gr} ≈ –4.6 eV (neutral) to Φ_{p-Gr} ≈ –4.86 eV (p-doped).[29,46] The HOMO and LUMO values for the biocompatible nitrocellulose molecules on top of graphene as well as for the phenylalanine and tyrosine amino acids in the kidney tissue below graphene (plus other amino acids) were obtained from literature data.[49–51] These HOMO/LUMO levels and their energy differences relative to E_F of p-type graphene ($\Delta E_{HF}/\Delta E_{LF}$) are listed in Table S2, Supporting Information. The smaller ΔE_{HF} of ≈0.09, ≈–0.34, and ≈–0.29 for top and bottom molecules in our case indicate a favorable energy-level alignment of HOMO with p-doped graphene, which fits very well with the Raman findings.

Despite the heterogeneous molecular structure of tissues and large biomolecules like nucleobases, peptides, and proteins, their constituent amino acids are considered the basic building blocks interacting with GBMs.[23,41,42] Amino acids containing aromatic rings (phenylalanine, tryptophan, and tyrosine) were shown to be strongly adsorbed in a parallel orientation on the surface of GBMs via π–π interactions.[52] However, we observed relatively moderate GERS factors for the Raman peaks of tyrosine (≈2.1, ≈2.42) and phenylalanine (≈5.24) as displayed in Figure 2c although their symmetry is close to that of graphene as revealed by the chemical structures in Figure 3f. While in previous theoretical and experimental investigations amino acids are let to relax and reach their equilibrium positions over graphene,[45,53,54] in our configuration the kidney tissues and hence the amino acids are first fixed on a non-graphitic surface and then graphene is transferred atop. We believe that this reversed geometry allows less freedom of movement and therefore leads to larger distances

between graphene and amino acids, which can explain the limited EFs. As expected, the molecules on top of graphene experience little geometrical constrains that combined with their chemical structure (Figure 3f) promote arrangement in more effective equilibrium configurations resulting in a smaller separation and a higher GERS figure of ≈10.1 (Figure 2c).

The molecular structural variability of amino acids enables not only different binding affinities to GBMs through non-covalent van der Waals, π–π stacking, and hydrophobic interactions, but also distinct electronic structures.[41] The latter leads to specific HOMO and LUMO energy levels for amino acids that can be used as orientation values to tune the E_F position of graphene through external p- or n-type doping for efficient charge transfer in prospective studies.[29,51] This perspective is presented in Figure 3g with the corresponding data and abbreviations being summarized in Table S3, Supporting Information. It shows that by varying the carrier concentration in graphene, its Fermi level and thus work function can in principle be shifted such that an alignment either to the HOMO or LUMO energies of amino acids is achievable (green and light orange open circles, respectively). A closer energy level alignment can promote additional charge transfer between molecules and graphene and thus increased FLQ and Raman enhancement.[20,22,32] Nevertheless, more research is needed to account for the hybridization of the electronic states in every hybrid biological system that can modify the HOMO and LUMO energies to some extent relative to isolated amino acids.[51]

2.5. Comparison with Photobleaching

The use of various chemicals to reduce inherent autofluorescence of tissue sections generates additional Raman bands that overlap with those of tissues making a straightforward materials separation challenging. Photobleaching represents a label-free FLQ alternative, which is based on prolonged light irradiation causing a photochemical transformation of fluorophore molecules in biological entities.[33,34,55] We exposed the kidney tissues without graphene to three laser excitation wavelengths (457, 532, and 660 nm) and measured the time evolution of partial FL/Raman spectra every 2 min for 40 min as displayed in **Figure 4**. The Raman peaks superimposed on the autofluorescence background are barely (457 nm) or better (532, 660 nm) visible, along with the laser line at 0 cm^{-1} and the cut-off of the edge filters. In particular, more and well-defined tissue Raman features were obtained with the red laser (Figure 4c) mainly because the 660 nm excitation and the emitted Raman light at higher wavelengths are located on the decreasing tail of the FL curve resulting in less background signal (Figure 2a). Therefore, all Raman measurements in this paper were performed with the red laser.

Note in Figure 4d that the anticipated decrease in the FL background (blue, green, red curves with squares) coexists with an overall reduction in Raman intensities as exemplified for the phenylalanine peak at ≈1001 cm^{-1} (red curve with triangles). Given the moderate employed laser powers and the similar

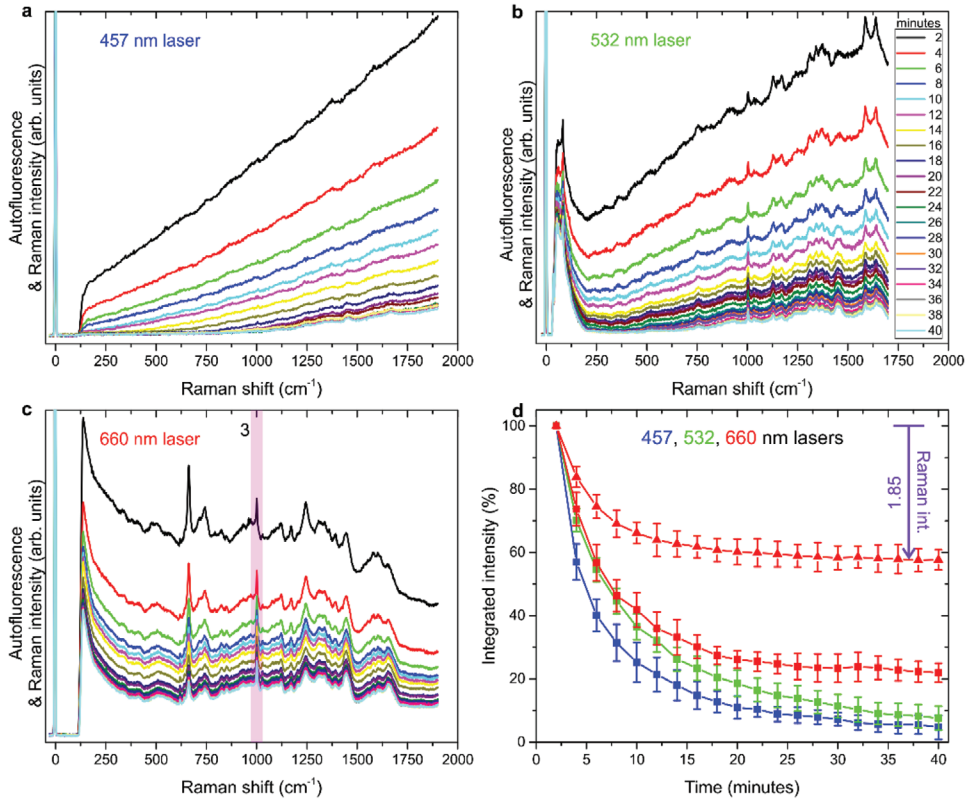

Figure 4. a–c) Photobleaching treatments of the kidney tissue without graphene excited with three laser wavelengths: 457, 532, and 660 nm. Partial fluorescence/Raman spectra emitted by the kidney tissue were recorded every 2 min for a total time of 40 min. d) The reduction in the autofluorescence background (curves with squares) is accompanied by the decrease in Raman intensities (curve with triangles), the latter being illustrated for the phenylalanine Raman band (peak 3 in (c) and Figure 2b,c).

measured spectral responses over time, we attribute these results to slight laser-induced changes in the structure of biomolecules because of the extended laser irradiation affecting the tissue integrity. In this context, our approach to exploit monolayer graphene in hybrid biomolecular systems outlines its multi-role as large contact and loading area for the biomolecules below and above graphene, respectively (Figure 1), as well as concomitant FLQ and Raman enhancement platform (Figure 2a,c). Moreover, the kidney tissue and graphene layer preserve their structural integrity, the latter showing virtually constant, low defect densities due to non-covalent interface interactions, which enable both qualitative (Figures 2d–f, 3b–e) and quantitative (Figure 3a) strain and doping analyses. Thus, the combined graphene-induced FLQ and double-sided GERS effects demonstrated in this work constitute an important progress over standard photobleaching. However, we speculate that the use of GBMs and/or photobleaching to reduce the autofluorescence background of biological materials will depend on the application.

3. Conclusion

In summary, we have systematically studied hybrid biomolecular-graphene structures by following the evolution of micro-Raman and FL spectra in subsequent layered materials. It is found that the graphene-enhanced Raman scattering effect occurs for biomolecules in intimate contact with graphene on both sides, an advancement over typical GERS that we coined double-sided GERS. The interaction with graphene also leads to quenching of autofluorescence originating from the kidney tissue. The strength of double-sided GERS and FLQ was explained by the capability of biocompatible nitrocellulose molecules and amino acids in the kidney tissue to achieve certain equilibrium arrangements when adsorbed on graphene and located below it, respectively. These geometries can result in different distances between molecules and graphene that along with their symmetry and relative energy level alignment impact the charge transfer among them.

Compared to normal photobleaching without graphene, we observed the expected reduction in the FL background, but this comes at the cost of some laser-induced structural changes of biomolecules in the kidney tissue. This is indicated by decreasing tissue Raman peak intensities upon prolonged laser irradiation, which is in contrast to the Raman enhancements caused by the presence of graphene. Moreover, we theoretically show that by tuning the hole or electron concentration in graphene through doping, the Fermi level of graphene can be aligned to the HOMO or LUMO energies of amino acids as the key constituents of biological entities interacting with GBMs. This opens the way toward engineering graphene-based drug delivery systems including optimized Raman/FL imaging and sensing through non-covalent interactions.

4. Experimental Section

Human Kidney Tissue: Cryo-fixed archival human kidney tissue was provided by the Department of Nephropathology at Friedrich-Alexander-University of Erlangen-Nürnberg (FAU). Sections of ≈5 µm thickness were transferred on Ni-coated Si wafers followed by air drying overnight. The kidney showed no evidence of renal disease and was obtained from distant portion of a kidney surgically excised because of the presence of a localized neoplasm. The use of kidney biopsies was approved by the Ethics Committee of the FAU, waiving the need for retrospective consent for the use of archived rest material (reference number 4415).

Graphene Transfer: Predominantly single-layer graphene films were grown by chemical vapor deposition (CVD) on copper foils using a two-step process as described previously.[29] The graphene-on-copper samples were spin-coated with a collodion solution (2% nitrocellulose in a 1:1 mixture of diethyl ether and ethanol) at 2500 rpm for 45 s and let dry in air for 5 min. Oxygen plasma was employed to etch graphene from the uncovered side of the copper foils. Afterward, the copper foils were etched in a solution of ammonium peroxo-disulfate (2.5 wt%) and deionized water for 24 h. The remaining nitrocellulose-graphene layers were rinsed in deionized water and transferred onto kidney tissue/Ni/Si and SiO_2/Si reference substrates, which were then let dry in air for 2 h at an inclined angle. Finally, most of the biocompatible nitrocellulose layer was removed by submerging the samples in a 2:1 mixture of diethyl ether and ethanol for 24 h, followed by a short deep cleaning in deionized water. Note that this new collodion-mediated transfer method of CVD graphene does not require heating, contrary to the commonly used PMMA-assisted transfer procedure, that is, the structural and chemical properties of the kidney tissue, graphene, and biomolecules were not altered by any thermal annealing step.[29] Moreover, the cryo-fixed human kidney tissues were prepared without staining and paraffin embedding matrix to avoid every damage and spectral artifacts, thus ensuring reliable and reproducible FL and Raman spectra from the kidney tissue.[25,56,57]

FL and Raman Measurements: A LabRam HR800 spectrometer from Horiba Scientific was used in a backscattering geometry under ambient conditions at room temperature. Ten FL emission spectra of kidney tissue without and with monolayer graphene on top were excited and collected at different locations through a 50× objective (numerical aperture (NA) 0.8, Nikon) employing a 457 nm laser wavelength, a probing macro-beam[58] of 100 × 100 µm^2, and a laser power on the sample surface of ≈165 µW. Two mean FL spectra were then calculated and compared in Figure 2a. Three Raman maps (60 × 60 µm^2) for each combination of materials including Ki/Ni, Mo/Gr/Ni, Mo/Gr/Ki/Ni, and Mo/Gr/SiO_2 reference were acquired at distinct positions using a 100× objective (NA 0.9, Olympus), a laser excitation wavelength of 660 nm, a probing micro-beam diameter of ≈1 µm, a step size of ≈0.7 µm, and a laser power of ≈1.28 mW. Examples of Raman intensity maps of the same area along with their single Gaussian fitted histograms indicating uniform spatial deviations in the molecular structure of the kidney tissue below graphene and molecule coverage on top of graphene are displayed in Figure S4, Supporting Information. Such variations were inherent to the kidney tissue and non-covalent coverage with transfer molecules on large-area graphene. Next, mean Raman spectra were computed and shown in Figure 2b and Figures S2 and S3, Supporting Information after and before FL background subtraction, respectively. The mean FL/Raman spectra were corrected for the ≈4.6% light absorption in single-layer graphene both in excitation and detection.[59] By fitting all spectra individually, correlative 2D plots[29] were also obtained and displayed in Figure 3a–e. Here, for better visualization, the data points in histogram bins with < 50 counts were removed, corresponding to < 4% from total.

Photobleaching: The kidney tissue samples were irradiated through a 50× objective (NA 0.8, Nikon) with 457, 532, and 660 nm laser wavelengths employing a probing macro-beam of 100 × 100 µm^2 and laser powers of ≈165 µW, 1.76 mW, and 1.28 mW. Three exposures were performed for each wavelength at different positions, each exposure lasted 40 min and every 2 min partial FL/Raman spectra were measured, which are shown and analyzed in Figure 4. Note that the used laser powers adjustable by filters did not result in visible structural damage as confirmed by optical microscopy and FL/Raman spectra with alike features.

Supporting Information

Supporting Information is available from the Wiley Online Library or from the author.

Acknowledgements

G.S. and S.H.C. acknowledge the financial support from the European Union within the research projects npSCOPE and 4D+nanoSCOPE. C.D. and K.A. were supported by the German Research Foundation (DFG), project number 387509280, SFB 1350 TP C2. This research was done in the "COPERIMOplus" initiative and supported by the Fraunhofer "Internal Programs" under Grant No. Anti-Corona 840266.

Open access funding enabled and organized by Projekt DEAL.

Conflict of Interest

The authors declare no conflict of interest.

Data Availability Statement

The data that support the findings of this study are available in the supplementary material of this article, and from the corresponding author upon reasonable request.

Keywords

amino acids, fluorescence quenching, graphene-enhanced Raman scattering, kidney tissues, photobleaching

Received: March 30, 2021
Revised: June 18, 2021
Published online: July 31, 2021

[1] H. Zhang, T. Fan, W. Chen, Y. Li, B. Wang, *Bioact. Mater.* **2020**, *5*, 1071.
[2] Z. Liu, S. Li, X. Xia, Z. Zhu, L. Chen, Z. Chen, *Small Methods* **2020**, *4*, 1900440.
[3] Y. Tao, H. F. Chan, B. Shi, M. Li, K. W. Leong, *Adv. Funct. Mater.* **2020**, *30*, 2005029.
[4] H. Y. Mao, S. Laurent, W. Chen, O. Akhavan, M. Imani, A. A. Ashkarran, M. Mahmoudi, *Chem. Rev.* **2013**, *113*, 3407.
[5] K. T. Nguyen, Y. Zhao, *Rev. Cell Biol. Mol. Med.* **2015**, *1*, 386.
[6] G. Hong, S. Diao, A. L. Antaris, H. Dai, *Chem. Rev.* **2015**, *115*, 10816.
[7] G. Shim, M.-G. Kim, J. Y. Park, Y.-K. Oh, *Adv. Drug Delivery Rev.* **2016**, *105*, 205.
[8] J. Lin, X. Chen, P. Huang, *Adv. Drug Delivery Rev.* **2016**, *105*, 242.
[9] G. Sarau, B. Lahiri, P. Banzer, P. Gupta, A. Bhattacharya, F. Vollmer, S. Christiansen, *Adv. Opt. Mater.* **2013**, *1*, 151.
[10] B. Kann, H. L. Offerhaus, M. Windbergs, C. Otto, *Adv. Drug Delivery Rev.* **2015**, *89*, 71.
[11] J. Bartelmess, S. J. Quinn, S. Giordani, *Chem. Soc. Rev.* **2015**, *44*, 4672.
[12] S. Sun, P. Wu, *Phys. Chem. Chem. Phys.* **2011**, *13*, 21116.
[13] X. Ma, Q. Qu, Y. Zhao, Z. Luo, Y. Zhao, K. W. Ng, Y. Zhao, *J. Mater. Chem. B* **2013**, *1*, 6495.
[14] Y. Wang, L. Polavarapu, L. M. Liz-Marzán, *ACS Appl. Mater. Interfaces* **2014**, *6*, 21798.
[15] A. Povolotckaia, D. Pankin, Y. Petrov, A. Vasileva, I. Kolesnikov, G. Sarau, S. Christiansen, G. Leuchs, A. Manshina, *J. Mater. Sci.* **2019**, *54*, 8177.
[16] K. Kneipp, H. Kneipp, M. Moskovits, *Surface-Enhanced Raman Scattering: Physics and Applications*, Springer-Verlag, Berlin, Heidelberg **2006**.
[17] X. Ling, S. Huang, S. Deng, N. Mao, J. Kong, M. S. Dresselhaus, J. Zhang, *Acc. Chem. Res.* **2015**, *48*, 1862.
[18] N. Zhang, L. Tong, J. Zhang, *Chem. Mater.* **2016**, *28*, 6426.
[19] E. B. Barros, M. S. Dresselhaus, *Phys. Rev. B* **2014**, *90*, 035443.
[20] S. Huang, X. Ling, L. Liang, Y. Song, W. Fang, J. Zhang, J. Kong, V. Meunier, M. S. Dresselhaus, *Nano Lett.* **2015**, *15*, 2892.
[21] L. Xie, X. Ling, Y. Fang, J. Zhang, Z. Liu, *J. Am. Chem. Soc.* **2009**, *131*, 9890.
[22] A. Kasry, A. A. Ardakani, G. S. Tulevski, B. Menges, M. Copel, L. Vyklicky, *J. Phys. Chem. C* **2012**, *116*, 2858.
[23] S. Li, A. N. Aphale, I. G. Macwan, P. K. Patra, W. G. Gonzalez, J. Miksovska, R. M. Leblanc, *ACS Appl. Mater. Interfaces* **2012**, *4*, 7069.
[24] W. Lin, B. Tian, P. Zhuang, J. Yin, C. Zhang, Q. Li, T. M. Shih, W. Cai, *Nano Lett.* **2016**, *16*, 5737.
[25] L. E. Kamemoto, A. K. Misra, S. K. Sharma, M. T. Goodman, H. Luk, A. C. Dykes, T. Acosta, *Appl. Spectrosc.* **2010**, *64*, 255.
[26] A. T. Lewis, R. Gaifulina, M. Isabelle, J. Dorney, M. L. Woods, G. R. Lloyd, K. Lau, M. Rodriguez-Justo, C. Kendall, N. Stone, G. M. Thomas, *J. Raman Spectrosc.* **2017**, *48*, 119.
[27] R. A. Hall, in *Protein-Protein Interactions*, Vol. *261*, Humana Press, Totowa, NJ **2004**, pp. 167.
[28] B. T. Kurien, R. H. Scofield, *Methods Mol. Biol.* **2009**, *536*, 367.
[29] G. Sarau, M. Heilmann, M. Bashouti, M. Latzel, C. Tessarek, S. Christiansen, *ACS Appl. Mater. Interfaces* **2017**, *9*, 10003.
[30] P. Nguyen, V. Berry, *J. Phys. Chem. Lett.* **2012**, *3*, 1024.
[31] X. Ling, J. Zhang, *J. Phys. Chem. C* **2011**, *115*, 2835.
[32] N. Zhang, J. Lin, W. Hu, S. Zhang, L. Liang, R. Wang, X. Luo, Y. Luo, X. Qiu, J. Zhang, L. Tong, *Nano Lett.* **2019**, *19*, 1124.
[33] T. Erben, R. Ossig, H. Y. Naim, J. Schnekenburger, *Histopathology* **2016**, *69*, 406.
[34] Y. Sun, H. Yu, D. Zheng, Q. Cao, Y. Wang, D. Harris, Y. Wang, *Arch. Pathol. Lab. Med.* **2011**, *135*, 1335.
[35] A. W. Auner, R. E. Kast, R. Rabah, J. M. Poulik, M. D. Klein, *Pediatr. Surg. Int.* **2013**, *29*, 129.
[36] D. S. Moore, S. D. McGrane, *J. Mol. Struct.* **2003**, *661–662*, 561.
[37] A. C. Ferrari, D. M. Basko, *Nat. Nanotechnol.* **2013**, *8*, 235.
[38] J. Müller-Deile, G. Sarau, A. M. Kotb, C. Jaremenko, U. E. Rolle-Kampczyk, C. Daniel, S. Kalkhof, S. H. Christiansen, M. Schiffer, *Sci. Rep.* **2021**, *11*, 4577.
[39] S. Stewart, P. M. Fredericks, *Spectrochim. Acta, Part A* **1999**, *55*, 1641.
[40] W. Xu, N. Mao, J. Zhang, *Small* **2013**, *9*, 1206.
[41] H. Vovusha, S. Sanyal, B. Sanyal, *J. Phys. Chem. Lett.* **2013**, *4*, 3710.
[42] X. Zou, S. Wei, J. Jasensky, M. Xiao, Q. Wang, C. L. Brooks, Z. Chen, *J. Am. Chem. Soc.* **2017**, *139*, 1928.
[43] B. Keisham, A. Cole, P. Nguyen, A. Mehta, V. Berry, *ACS Appl. Mater. Interfaces* **2016**, *8*, 32717.
[44] A. C. R. Fernández, N. J. Castellani, *ChemPhysChem* **2017**, *18*, 2065.
[45] S. J. Rodríguez, L. Makinistian, E. A. Albanesi, *Appl. Surf. Sci.* **2017**, *419*, 540.
[46] A. Das, S. Pisana, B. Chakraborty, S. Piscanec, S. K. Saha, U. V. Waghmare, K. S. Novoselov, H. R. Krishnamurthy, A. K. Geim, A. C. Ferrari, A. K. Sood, *Nat. Nanotechnol.* **2008**, *3*, 210.
[47] J. E. Lee, G. Ahn, J. Shim, Y. S. Lee, S. Ryu, *Nat. Commun.* **2012**, *3*, 1024.
[48] F. Ding, H. Ji, Y. Chen, A. Herklotz, K. Dörr, Y. Mei, A. Rastelli, O. G. Schmidt, *Nano Lett.* **2010**, *10*, 3453.
[49] S. M. Romanova, A. M. Madyakina, A. R. Khamatgalimov, S. V. Fridland, M. V. Khuzeev, *Russ. J. Gen. Chem.* **2014**, *84*, 758.
[50] M. F. Zaki, A. M. Ali, R. M. Amin, *J. Adhes. Sci. Technol.* **2017**, *31*, 1314.
[51] M. Oda, T. Nakayama, *Jpn. J. Appl. Phys.* **2008**, *47*, 3712.

[52] S. S. K. Mallineni, J. Shannahan, A. J. Raghavendra, A. M. Rao, J. M. Brown, R. Podila, *ACS Appl. Mater. Interfaces* **2016**, *8*, 16604.
[53] C. Rajesh, C. Majumder, H. Mizuseki, Y. Kawazoe, *J. Chem. Phys.* **2009**, *130*, 124911.
[54] S. Pandit, M. De, *J. Phys. Chem. C* **2017**, *121*, 600.
[55] Y. Zhao, Y. Yamaguchi, C. Liu, M. Li, X. Dou, *Spectrochim. Acta, Part A* **2019**, *216*, 202.
[56] C. A. Lieber, M. H. Kabeer, *J. Pediatr. Surg.* **2010**, *45*, 549.
[57] B. Brozek-Pluska, J. Musial, R. Kordek, E. Bailo, T. Dieing, H. Abramczyk, *Analyst* **2012**, *137*, 3773.
[58] G. Sarau, A. Bochmann, R. Lewandowska, S. Christiansen, in *Advanced Aspects of Spectroscopy*, InTech, London **2012**, pp. 221.
[59] R. R. Nair, P. Blake, A. N. Grigorenko, K. S. Novoselov, T. J. Booth, T. Stauber, N. M. R. Peres, A. K. Geim, *Science* **2008**, *320*, 1308.